

Cryogenic Noble Gas Separation without Distillation: The Effect of Carbon Surface Curvature on Adsorptive Separation

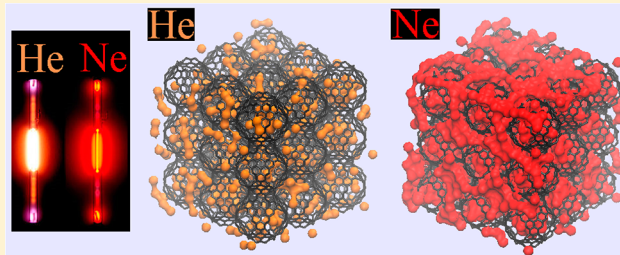
Piotr Kowalczyk,*† Piotr A. Gauden,‡ and Artur P. Terzyk‡

†Nanochemistry Research Institute, Department of Chemistry, Curtin University of Technology, P. O. Box U1987, Perth, 6845 Western Australia, Australia

‡Department of Chemistry, Physicochemistry of Carbon Materials Research Group, Nicolaus Copernicus University, Gagarin Street 7, 87-100 Torun, Poland

ABSTRACT: Applying a novel self-consistent Feynman–Kleinert–Sesé variational approach (Sesé, L. M. *Mol. Phys.* **1999**, *97*, 881–896) to quantum thermodynamics and the ideal adsorbed solution theory, we studied adsorption and equilibrium separation of ^{20}Ne – ^4He mixtures in carbonaceous nanomaterials consisting of flat (graphite-like lamellar nanostructures) and curved (triply periodic minimal carbon surfaces) nanopores at 77 K. At the infinite mixture dilution, Schwarz P-carbon and Schoen G-carbon sample represents potentially efficient adsorbents for equilibrium separation of ^{20}Ne – ^4He mixtures.

The equilibrium selectivity of ^{20}Ne over ^4He ($\alpha_{\text{Ne}-\text{He}}$) computed for Schwarz P-carbon and Schoen G-carbon sample is very high and reaches 219 and 163 at low pore loadings, respectively. Graphite-like lamellar nanostructures with interlamellar spacing (Δ) less than 0.6 nm are also potential adsorbents for equilibrium separation of ^{20}Ne – ^4He mixtures at cryogenic temperatures. Here, $\alpha_{\text{Ne}-\text{He}}$ of 80 is predicted for $\Delta = 0.46$ nm at low pore loadings. The quantum-corrected molar enthalpy of ^{20}Ne adsorption strongly depends on the curvature of carbon nanopores. For Schwarz P-carbon sample, it reaches 8.2 kJ mol⁻¹, whereas for graphite-like lamellar nanostructures the maximum enthalpy of ^{20}Ne physisorption of 5.6 kJ mol⁻¹ is predicted at low pore loadings. In great contrast, the quantum-corrected molar enthalpy of ^4He adsorption is only slightly affected by the curvature of carbon nanopores. The maximum heat released during the ^4He physisorption is 3.1 (Schwarz P-carbon) and 2.7 kJ mol⁻¹ (graphite-like lamellar nanostructure consisting of the smallest flat carbon nanopores). Interestingly, for all studied carbonaceous nanomaterials consisting of curved/flat nanopores, $\alpha_{\text{Ne}-\text{He}}$ computed for the equimolar composition of ^{20}Ne – ^4He gaseous phases is still very high at total mixture pressure up to 1 kPa. This circumstance is indicative of the possibility of carrying out the adsorption separation of ^{20}Ne – ^4He mixtures at $p_t < 1$ kPa and 77 K that do not require high-energy consumption. Presented potential models and simulation methods will further enhance the accuracy of modeling of confined inhomogeneous quantum fluids at finite temperatures.



I. INTRODUCTION

High-purity noble gases, including ^{20}Ne and ^4He , are very important for lasers, light bulbs, scuba diving lights, etc.^{1–3} Apart from its use in fluorescent light fixtures, ^{20}Ne has also found application in high-energy physics and military.¹ On the other hand, liquid ^4He is an important cooling agent used in nuclear plants, basic scientific research, medical imaging, and other cryogenic systems.^{1–3} Because the electron shells of noble gases are completely filled, they are inert, that is, do not normally form chemical compounds.⁴ Moreover, ^{20}Ne and ^4He exhibit significant quantum effects throughout their liquid range.^{5–22} As has been shown by Beenakker et al.²³ and others,^{24–26} nanoscale confinement additionally impacts the space/momenta localization of quantum particles, which amplify the importance of quantum effects at finite temperatures. Thus, the accurate treatment of the phase behavior of these fluids under strong confinement must include quantum effects. Taking into account the quantum nature of ^{20}Ne and ^4He atoms, as well as their chemical inertness, we argue that the

separation of ^{20}Ne – ^4He mixtures is a challenging problem for both experimentalists and theoreticians.

^{20}Ne has been extracted from the atmosphere as a byproduct in air separation plants. Typical analysis of ^{20}Ne stream after complete H_2 removal consists of the following: N_2 (70%), ^{20}Ne (23%), and ^4He (7%).¹ By passing the mixture at a pressure of around 50 bar through a reflux exchanger surrounded by a bath of liquid N_2 , it is fairly easy to remove the bulk of N_2 .¹ A bed of activated charcoal (or other ordinary porous carbon) can adsorb the remaining traces of N_2 .¹ In contrast to N_2 capture, the separation of ^{20}Ne from ^4He is very difficult and expensive. Because the critical temperature of ^{20}Ne is 44.41 K and that of ^4He is 5.2 K, the use of liquid H_2 as a refrigerant is necessary. Meissner succeeded in separating ^{20}Ne – ^4He mixture on a fairly large scale by using H_2 in the early 1930s.¹ This treatment,

Received: June 7, 2012

Revised: August 24, 2012

Published: August 26, 2012



however, presents a problem because the boiling point of H₂ is 20.4 K and that of ²⁰Ne is 27.2 K. The triple point of ²⁰Ne on the other hand is 24.6 K, which is above the boiling point of H₂. Thus, care has to be exercised to make sure that the ²⁰Ne does not solidify and block the tube (see ref 1 for other details). The separation factor, $\alpha_{\text{Ne-He}}$, which is simply relative volatility for distillation, is not high for cryogenic separation of ²⁰Ne–⁴He mixtures.¹ Therefore, novel concepts and technologies are needed in order to develop/improve the ²⁰Ne–⁴He separation processes.

In recovering of ²⁰Ne from ²⁰Ne–⁴He mixtures, the separation by adsorption systems seems to be a very attractive alternative to costly and energy-intensive cryogenic distillation operations.^{1–3} However, as pointed out by Ruthven and others,^{27–30} a *highly selective nanoporous material* is a key to achieve the high adsorption selectivity of ²⁰Ne over ⁴He. For equilibrium-driven separation, the intrinsic selectivity of nanoporous materials at infinite dilution of gaseous mixture is simply given by the ratio of the equilibrium constants (Henry's law constants), $\alpha_{\text{Ne-He}} = K_{\text{Ne}}/K_{\text{He}}$.^{31,32} It is expected that nanoporous material has the adsorption preference toward ²⁰Ne, i.e., $K_{\text{Ne}}/K_{\text{He}} > 1$. This is because the strength of the van der Waals interactions between adsorbed noble gases and nanoporous materials is higher for larger adsorbed atoms. Simply, as polarizability increases, dispersion forces also become stronger.⁴ Carbonaceous nanomaterials, including ordinary porous carbon, activated carbon fibers, ordered porous carbons, carbon nanotubes, and recently synthetized graphitic nanoribbons,^{33,34} are promising and fascinating nanostructures that can be potentially used in adsorption separation of ²⁰Ne–⁴He mixtures at 77 K (note that the selected operating temperature is a boiling point of N₂, which is easily achievable¹). These carbonaceous nanomaterials consist of various flat/curves nanopores that represent strong adsorption centers with high adsorption capacity.^{33,34} In order to optimize the $\alpha_{\text{Ne-He}}$, we need to understand the impact of the nanopore curvature on the cryogenic adsorption of noble gas mixtures. For graphite-like lamellar nanostructures we need to tune the interlamellar spacing in order to get high $\alpha_{\text{Ne-He}}$. As shown by Gogotsi and co-workers,³³ tunable nanoporous carbons can be produced from metallic carbides by chemically removing the metallic element, leaving a systematic array of pores on the nanometer level. How $\alpha_{\text{Ne-He}}$ varies with the curvature of carbon nanopores, what is the optimal interlamellar spacing for ²⁰Ne–⁴He mixture adsorptive separation, and how $\alpha_{\text{Ne-He}}$ varies with the total pressure of equimolar ²⁰Ne/⁴He mixtures at 77 K are key questions that we would like to answer, and this is the primary goal of the current work.

II. THEORY AND SIMULATION METHODS

II.a. Potential Models. To take into account quantum effects, such as zero-point energy and tunneling, both fluid–fluid (i.e., ⁴He–⁴He and ²⁰Ne–²⁰Ne) and solid–fluid (i.e., ⁴He–C, and ²⁰Ne–C) interactions were computed from the self-consistent variational Feynman–Kleinert–Sesé effective potential (FKS), given by (we used the notation from ref 35)

$$V_{\text{FKS}}(\beta, r) = \begin{cases} V_{\text{LJ}}(r) - \frac{1}{8}A^4(\beta, r)\nabla^4V_{\text{LJ}}(r) \\ + \frac{3}{\beta}\ln\left\{\frac{\sinh[\beta\hbar\Omega(\beta, r)/2\mu^{1/2}]}{\beta\hbar\Omega(\beta, r)/2\mu^{1/2}}\right\}, \\ \Omega^2 > 0 \\ V_{\text{LJ}}(r) - \frac{1}{8}A_{\text{GFH}}^4(\beta)\nabla^4V_{\text{LJ}}(r), \quad \Omega^2 = 0 \\ V_{\text{LJ}}(r) - \frac{1}{8}\bar{A}^4(\beta, r)\nabla^4V_{\text{LJ}}(r) \\ + \frac{3}{\beta}\ln\left\{\frac{\sin[\beta\hbar|\Omega(\beta, r)|/2\mu^{1/2}]}{\beta\hbar|\Omega(\beta, r)|/2\mu^{1/2}}\right\}, \\ \Omega^2 < 0 \end{cases} \quad (1)$$

where $\Omega^2(\beta, r)$, $a^2(\beta, r)$, and $V_{\text{LJ}}(r)$ are computed from³⁵

$$\Omega^2(\beta, r) = \frac{1}{3}\nabla^2V_{\text{LJ}}(r) + \frac{1}{6}a^2(\beta, r)\nabla^4V_{\text{LJ}}(r) \quad (2)$$

$$a^2(\beta, r) = \begin{cases} A^2(\beta, r) = \frac{1}{\beta\Omega^2(\beta, r)} \\ \left[\frac{\beta\hbar\Omega(\beta, r)}{2\mu^{1/2}}\cosh\left(\frac{\beta\hbar\Omega(\beta, r)}{2\mu^{1/2}}\right) - 1\right], \\ \Omega^2 > 0 \\ A_{\text{GFH}}^2(\beta) = \beta\hbar^2/12\mu, \quad \Omega^2 = 0 \\ \bar{A}^2(\beta, r) = \frac{1}{\beta\Omega^2(\beta, r)} \\ \left[\frac{\beta\hbar|\Omega(\beta, r)|}{2\mu^{1/2}}\cot\left(\frac{\beta\hbar|\Omega(\beta, r)|}{2\mu^{1/2}}\right) - 1\right], \\ \Omega^2 < 0 \end{cases} \quad (3)$$

$$V_{\text{LJ}}(r) = 4\varepsilon\left[\left(\frac{\sigma}{r}\right)^{12} - \left(\frac{\sigma}{r}\right)^6\right] \quad (4)$$

In the above equations, $\hbar = h/2\pi$ denotes Planck's constant, $\mu = m_1m_2/(m_1 + m_2)$ is the reduced mass, $\beta = (k_B T)^{-1}$ is the inverse of thermal energy, r denotes the distance between two interacting atoms, and the (12,6) Lennard-Jones (LJ) well-depth and collision diameter are given by ε and σ , respectively. For computing of ⁴He–⁴He interactions, we used the following LJ parameters: $\sigma = 0.2556$ nm, $\varepsilon/k_B = 10.22$ K.^{12,13} For computing of ²⁰Ne–²⁰Ne interactions, we adopted the following LJ parameters: $\sigma = 0.2789$ nm, $\varepsilon/k_B = 36.814$ K.¹⁰ Cross-interaction parameters were calculated using the Lorentz–Berthelot mixing rules:^{36–38} $\sigma_{\text{sf}} = (\sigma_{\text{ff}} + \sigma_{\text{ss}})/2$, $\varepsilon_{\text{sf}} = (\varepsilon_{\text{ff}}\varepsilon_{\text{ss}})^{1/2}$. As previously, for carbon atoms, we used LJ parameters from Steele's work: $\sigma = 0.34$ nm, $\varepsilon/k_B = 28.0$ K.^{39,40} For all computed interactions, we truncated the LJ potential at $r_c = 5\cdot\sigma$ (σ denotes the collision diameter for fluid–fluid interactions), without long-range correction. Note that LJ parameters for carbon were optimized for flat graphite surface. Slight polarization of noble gases adsorbed in curved graphitic-like nanopores may be expected. However, we argue that this effect increases the equilibrium selectivity as compared to our theoretical calculations. The ²⁰Ne atom has more electrons than

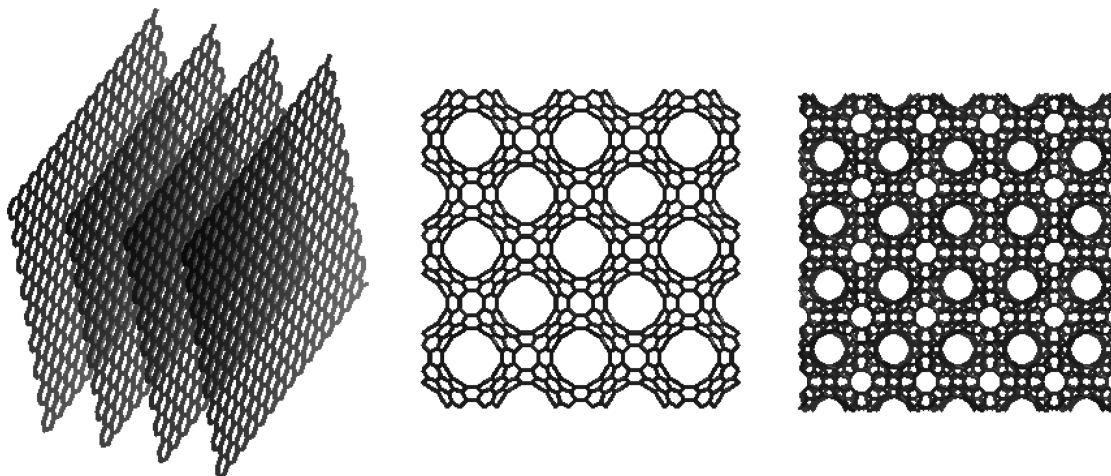


Figure 1. Graphite-like lamellar nanostructure (left panel), Schwarz P-carbon (middle panel), and Schoen G-carbon sample (right panel) used for GCMC simulations of ^4He and ^{20}Ne adsorption at 77 K.

the ^4He one. Thus, the electron cloud of the ^4He atom is less polarizable than the ^{20}Ne one.

In the studies of Sesé³⁵ and Feynman and Kleinert,⁴¹ it was shown that effective potential computed via the variational perturbation method is a powerful short-time approximation to the high-temperature density matrix. The approximate quantum equilibrium and thermodynamics properties computed for simple Boltzmannian quantum liquids (called semiclassical quantum liquids) at cryogenic temperatures, including liquid ^{20}Ne and ^4He , were in good agreement with the exact path integral calculations.³⁵ Moreover, it was shown that FKS effective potential represents a significant improvement over the frequently used Feynman–Hibbs approximations.³⁵ This is because the smearing of the classical potential by Gaussian wave packet is not only temperature-dependent but also distant-dependent (see pioneering work by Feynman and Kleinert⁴¹). When two quantum particles are separated, their high-temperature density matrix can spread more. On the other hand, if two quantum particles are very close, like in dense liquids, a given quantum particle cannot occupy the space of surrounding quantum particles, and since they are highly packed, the “volume” where the quantum particle can be is smaller. Therefore, the localization of quantum particle by hard cores of surrounding neighbors reduces the size of the Gaussian wave packet. In contrast, following the Feynman–Hibbs (FH) approximations,^{7–9} the size of the Gaussian wave packet (i.e., the spreading of the probability function in the positional space) does not change with the intermolecular distance, r , which is incorrect as $r \rightarrow 0$. Note that in the nanoscale confinement, the quantum particles are tightly packed and compressed by strong surface forces. Therefore, the FKS self-consistent treatment of quantum fluctuations is more realistic compared to FH approximations. In the current work eqs 1–4 were solved by using iterative methods with the converge criterion of 10^{-6} . Similar to Sesé calculations,³⁵ the starting point of iterations was $a_0^2 = A_{\text{GFH}}^2$, where $A_{\text{GFH}}^2 = \beta\hbar^2/12\mu$ is the Gaussian wave packed computed from the Feynman–Hibbs approximation (see ref 35 for other details).

II.b. Simulation Details. The molecular model of graphite-like lamellar nanostructure (see left panel of Figure 1) was constructed from perfect graphene sheets separated by distance Δ_g (Δ_g is the geometrical lamellar distance between carbon atom centers of opposing parallel graphene sheets). The

effective lamellar distance is simply $\Delta = \Delta_g - 0.34$ (Δ determines the space of the nanopore accessible for adsorbed atoms), where 0.34 nm is the collision diameter of C atom. A stack consisting of four graphene sheets was placed in a rectangular cuboid simulation box ($4 \times 4 \times L$ nm, where L was adjusted to keep the assumed interlamellar distance) with periodic boundary conditions and minimum image convention, for computing molecular interactions in x , y , and z directions.³⁶ Triply periodic carbon minimal surfaces³⁷ (Schwarz P-carbon and Schoen G-carbon) were modeled by fully atomistic representation (see middle and right panels of Figure 1). Periodically replicated triply periodic carbon minimal surfaces generated from the crystallographic structures of the unit cell³⁷ were place in a rectangular cuboid simulation box ($L_x \times L_y \times L_z$ nm, with three Cartesian dimensions >4 nm). Periodic boundary conditions and minimum image convention for computing molecular interactions in x , y , and z directions was used. ^{20}Ne and ^4He adsorption isotherms on model carbonaceous nanomaterials were simulated using the grand canonical Monte Carlo method (GCMC)^{36,38} at 77 K. Before GCMC simulations, we extracted the excess part of the chemical potential of studied adsorbates from Widom’s particle insertion method implemented in the canonical Monte Carlo ensemble.⁴² The bulk pressure corresponding to the chemical potential was computed from the virial theorem.³⁶ The tail corrections for the energy and pressure were added after simulation in the canonical ensemble.³⁶ Our computer GCMC experiment was designed to mimic an adsorption experiment. We started our GCMC simulation at very low pressure, around 10^{-23} kPa, and progressively increased the pressure of an adsorbate up to 1000 kPa. The final configuration of adsorbate molecules in studied carbonaceous nanomaterials computed at a lower pressure was taken as the starting one at higher pressure. To acquire the data in the GCMC simulation, we used at least 4×10^7 cycles for the system to reach equilibrium and another 4×10^7 cycles for the statistics collection. The Monte Carlo steps (in our simulations) consist of a grand canonical (Widom) insertion/deletion move and of a translation move. The details of these moves can be found elsewhere.³⁶ To attain microscopic reversibility and detailed balance, the translation/insertion/deletion move was selected with equal probability of 1/3. All simulated adsorption isotherms of ^4He and ^{20}Ne consisted of 120 points. For

graphite-like lamellar nanostructures, we covered the range of interlamellar distances $\Delta \in [0.46, 1.66]$ nm. For larger Δ , the equilibrium separation factor of ^{20}Ne over ^4He is monotonically decreasing. Therefore, we limited our investigations to $\Delta = 1.66$ nm. The structure of the unit cell for both Schwarz P-carbon and Schoen G-carbon sample was taken from Mackay and Terrones.³⁷

For both studied adsorbates, we computed the absolute value of adsorption form the following relation³⁸

$$\Gamma = \frac{\langle N \rangle}{M_C} \quad (5)$$

where $\langle N \rangle$ and M_C are the ensemble average of the number of adsorbed atoms and the total mass of carbon in the simulation box, respectively.

The enthalpy of adsorption per mole, i.e., the heat released during adsorption in studied carbonaceous nanomaterials, is computed from³⁸

$$\frac{q_{st}}{N_A} = \frac{5}{2} k_B T - \frac{\langle EN \rangle - \langle E \rangle \langle N \rangle}{\langle N^2 \rangle - \langle N \rangle^2} \quad (6)$$

where $\langle \dots \rangle$ denotes the ensemble average, N_A is Avogadro's number, and E is the sum of the kinetic and potential energies.

According to the FKS model, the total energy is given by³⁵

$$\begin{aligned} E = & \frac{3}{2} \langle N \rangle k_B T + \sum_{i < j}^N \beta \left\langle \frac{dV_{FKS,ij}^{\text{ff}}}{d\beta} \right\rangle + \sum_i^N \beta \left\langle \frac{dV_{FKS,i}^{\text{sf}}}{d\beta} \right\rangle \\ & + \dots \\ & \dots + \sum_{i < j}^N \langle V_{FKS,ij}^{\text{ff}} \rangle + \sum_i^N \langle V_{FKS,i}^{\text{sf}} \rangle \end{aligned} \quad (7)$$

where V_{FKS}^{ff} and V_{FKS}^{sf} , respectively, are the fluid–fluid and solid–fluid interaction potentials computed from the FKS effective potential. The first term of the right-hand side of eq 7 is the kinetic energy of classical particles, the second and third terms are required by the thermodynamic consistency, and the remaining terms are potential energies. Note that a second and third term in eq 7 represents quantum corrections to the kinetic energy (i.e., KEC terms in the ref 35). To the best of our knowledge, only classical enthalpy of ^{20}Ne and ^4He adsorption per mole has been published. This simplification is not acceptable for quantum atoms confined in strong external potential field (i.e., in narrow flat/curved carbon nanopores).

II.c. Ideal Adsorbed Solution Theory. The ideal adsorbed solution theory (IAST) due to Myers and Prausnitz is a well-established phenomenological approach used for predicting of multicomponent adsorption isotherms in nanoporous materials from experimental or simulated single-component adsorption data.^{43,44} The method is particularly suitable for the prediction of ^{20}Ne – ^4He mixture adsorption. This is because ^4He and ^{20}Ne have similar molecular sizes, and they are both interacting with the carbonaceous adsorbents via pure van der Waals forces.⁴ Following IAST theory, the following equation holds for each component of the studied mixture^{43,44}

$$p_t y_i = p_i^0(\Pi) x_i \quad (8)$$

where p_t is the total pressure of mixture, y_i and x_i denotes the molar fraction of i th mixture component in the bulk and the

pore phase, respectively, and $p_i^0(\Pi)$ is the pure adsorbed gas pressure for the i th mixture component.

For each mixture component, the value of the spreading pressure, Π in eq 8, is given by the following equation^{43,44}

$$\Pi^*(p^0) \equiv \frac{\Pi(p^0)A}{RT} = \int_0^{p^0} a(\zeta) d\zeta \quad (9)$$

where A is the surface area of the adsorbent, R is the universal gas constant, T denotes temperature, and a is the single-component absolute adsorption. As previously, to compute $\Pi^*(p^0)$, we described the single-component absolute adsorption isotherm by the following Toth equation^{30,45}

$$p = \left[\frac{b}{(a/a_m)^{-t} - 1} \right]^{1/t} \quad (10)$$

where a_m is the monolayer capacity and b and t are the Toth's model parameters.⁴⁵ Integration of eq 9 gives the following expression for the spreading pressure⁴⁴

$$\Pi^*(p^0) = a_m \left[\theta - \frac{\theta}{t} \ln(1 - \theta^t) - \sum_{j=1}^{\infty} \frac{\theta^{jt+1}}{jt(jt+1)} \right] \quad (11)$$

where $\theta = (a/a_m)$.

If we consider a binary mixture composed of species 1 and 2, the equality of the spreading pressure of each component in the adsorbed phase implies that⁴⁴

$$\Pi_{-1}^* \left(\frac{p_t y_1}{x_1} \right) = \Pi_{-2}^* \left(\frac{p_t y_2}{1 - x_1} \right) \quad (12)$$

This identity can be solved by standard numerical methods. Thus, for a given composition of the binary mixture in the bulk phase (p_t , y_1 , and y_2), we can predict the molar fractions of both mixture components in the adsorbed phase (x_1 and $x_2 \equiv 1 - x_1$). Correct description of single-component absolute adsorption isotherms is crucial for accurate prediction of mixture equilibria. As previously, we used a differential genetic algorithm to fit the theoretical Toth adsorption isotherms to the ^{20}Ne and ^4He adsorption isotherms simulated at 77 K.³⁰ The nonlinear problem given by eq 12 was solved by standard bisection method. Finally we would like to stress that IAST is a phenomenological theory based on classical surface thermodynamics, proved to work at higher temperatures. However, as reported by Johnson et al.,⁴⁶ IAST correctly reproduced the exact equilibrium separation factor for H_2 – T_2 mixtures adsorbed in narrow carbon nanotubes up to moderate pore loadings at 20 K (see Figure 7 in ref 46). Because we study the adsorption and separation of heavier atoms at 77 K, we are confident that IAST theory provides a correct description of ^{20}Ne – ^4He mixture adsorption at low and moderate pore loadings.

III. RESULTS AND DISCUSSION

Before the systematic study of the ^4He and ^{20}Ne adsorption in triply periodic minimal carbon surfaces and graphite-like lamellar nanostructures at 77 K, we checked the accuracy and consistency of the FKS model against known bulk properties. The behavior of the a^2 variational parameter for ^4He and ^{20}Ne at selected cryogenic temperatures is displayed in Figure 2. As expected, for each temperature, there are two asymptotic limits: $a^2 \rightarrow 0$ as $r \rightarrow 0$, and $a^2 \rightarrow A_{\text{GHF}}^2$ as $r \rightarrow \infty$. The first asymptotic

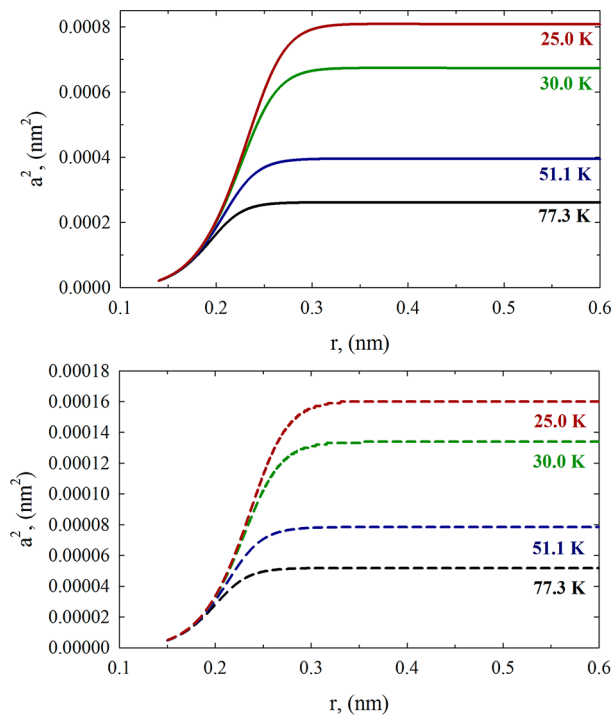


Figure 2. Behavior of the a^2 variational parameter (i.e., the size of the Gaussian wave packet smearing the classical LJ potential) for ^4He (upper panel) and ^{20}Ne (bottom panel) at selected temperatures (i.e., 77.3, 51.1, 30.0, and 25.0 K).

limit tells us that the size of the Gaussian wave packet is reduced when the quantum particles are getting closer. Following the quantum-classical isomorphism (see Chandler and Wolynes⁴⁷), the cyclic polymers quantizing particles are shrinking because of their localization in positional space. The second asymptotic limit tells us that the size of the Gaussian wave packet does not depend on r , when the quantum particles are far apart. Furthermore, as is theoretically justified, the asymptotic value of a^2 is A_{GHF}^2 (i.e., Gaussian wave packet computed from the Feynman–Hibbs approximation). For example, for ^4He at 77.3 K, $A_{\text{GHF}}^2 = 0.00026 \text{ nm}^2$, whereas for ^{20}Ne at 77.3 K, $A_{\text{GHF}}^2 = 0.00005 \text{ nm}^2$ (compare both values with the results displayed in Figure 2). From a practical point of view, we notice that for both ^4He and ^{20}Ne , the Feynman–Hibbs limit is achieved for $r \approx 0.4 \text{ nm}$, which is fully consistent with the pioneering work by Sesé.³⁵ Note, however, that quantum particles adsorbed in narrow ultramicropores are tightly packed and compressed by the external field and mutual interactions. The intermolecular distance between adsorbed quantum particles is often lower than 0.4 nm, especially at the pore saturation. Therefore, we concluded that for dense adsorbed phases consisting of quantum particles at cryogenic temperatures, the FKS approximation to the high-temperature density matrix is more realistic compared to commonly used FH approximations.

The reproduction of the experimental $^4\text{He}/^{20}\text{Ne}$ equation of state (EOS) at 77 K and pressures up to 3000 kPa is presented in Figure 3a. The agreement between experimental measurements and Monte Carlo simulations is very good. Interestingly, below 1000 kPa, the EOS for both studied adsorbates is the same. Above 1000 kPa, the ^{20}Ne density is higher compared to the ^4He one, which is a consequence of the stronger fluid–fluid interactions. To get more insight into the thermodynamic

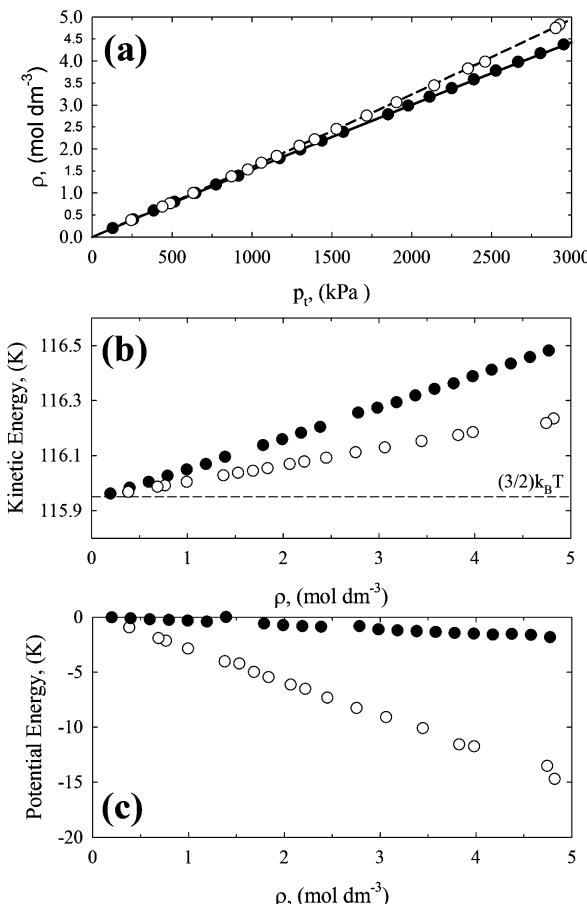


Figure 3. (a) Variation of the ^4He (black circles) and ^{20}Ne (open circles) density with pressure at 77 K computed from the FKS method and measured experimentally⁴⁸ (solid and dashed line). (b, c) Variation of the ^4He (black circles) and ^{20}Ne (open circles) kinetic and potential energy with density at 77 K computed from the FKS method, respectively. The classical kinetic energy is given by the dashed line in panel (b).

properties of ^4He and ^{20}Ne in the bulk phase at 77 K, we computed the variation of the mean kinetic and potential energy with the bulk density (see Figure 3b and 3c). A couple of things are immediately apparent: quantum fluctuations raise the mean kinetic energy of both adsorbates with increasing density, and the mean ^4He kinetic energy is always higher than the ^{20}Ne one (note that ^4He is lighter compared to ^{20}Ne). At very low densities, the mean kinetic energy values computed for ^4He and ^{20}Ne approach the classical limit. Moreover, we observe a linear increase in the mean kinetic energy with increasing density. This linear dependence derives from the low-density range studied here.¹¹ As would be expected, the mean ^{20}Ne potential energy is always lower than the ^4He one.

Figure 4 displays ^{20}Ne and ^4He adsorption isotherms at 77 K computed from GCMC simulations. We used a logarithmic scale to highlight the region of low pressures. For ^{20}Ne , all computed adsorption isotherms conform to type I according to the International Union of Pure and Applied Chemistry classification (IUPAC).⁴⁹ The type I isotherm corresponds to the so-called Langmuir isotherm. In the case of physical adsorption, the type I isotherm occurs for micropores where atoms are adsorbed by micropore filling which has been actively studied in adsorption science.⁴⁹ Interestingly, Schwarz P-carbon and Schoen G-carbon samples start to adsorb ^{20}Ne at very low

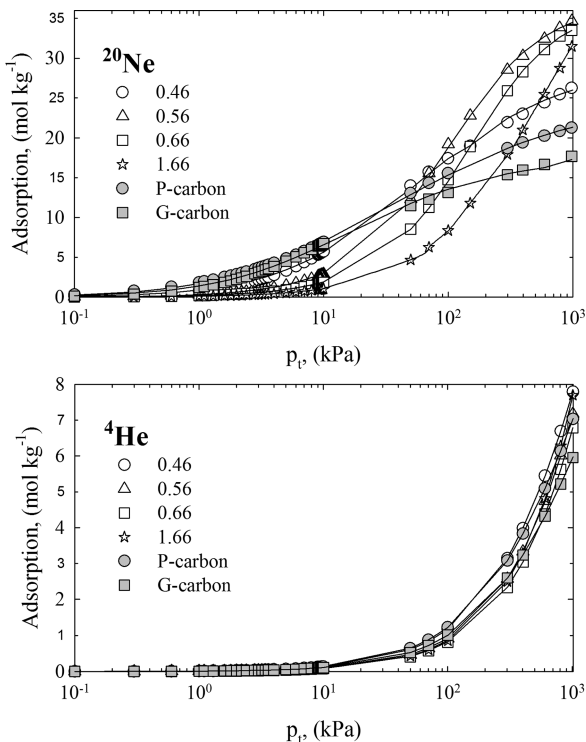


Figure 4. Adsorption isotherms of ^4He (bottom panel) and ^{20}Ne (upper panel) in Schwarz P-carbon, Schoen G-carbon, and selected graphite-like lamellar nanostructures at 77 K. Solid lines present the fitting of the three-parametric Toth adsorption model to simulated adsorption isotherms (symbols). The interlamellar distances, Δ , are displayed on the plots.

pressures, i.e., for $p_t < 1$ kPa. This is a consequence of the enhanced solid–fluid potential in narrow curved carbon nanopores (see Figure 5). Graphite-like lamellar nanostructures are able to adsorb ^{20}Ne at higher pressures, which indicates a weaker adsorption field in flat carbon nanopores. Packing of ^{20}Ne molecules in carbonaceous nanopores affected the curvature of computed isotherms (see Figure 4). For ^4He , all computed adsorption isotherms are characterized by significantly lower curvature as compared to ^{20}Ne . What is more important, we noticed that the curvature of carbon nanopores is not affecting the ^4He adsorption significantly. Regardless of different carbon nanopore size and geometry, all simulated ^4He adsorption isotherms are very similar (see Figure 4). Next, we found that all studied carbonaceous nanomaterials are able to adsorb ^4He at pressures above 10 kPa at 77 K. The adsorption capacity for ^4He is significantly lower as compared to ^{20}Ne ($\sim 5\text{--}6$ times). This indicates weak ^4He –carbon interactions at 77 K.

Figures 6 and 7 present the dependence of the quantum-corrected and classical enthalpy per mole upon ^4He and ^{20}Ne loading for Schwarz P-carbon, Schoen G-carbon, and selected graphite-like lamellar nanostructures. First, we notice that the quantum-corrected enthalpy of ^4He and ^{20}Ne adsorption is always lower than the classical one. Quantum fluctuations increase the kinetic energy of light particles that reduce the binding energy and further the heat realized during the adsorption of studied atoms. For lighter atoms and nanomaterials consisting of narrow carbon nanopores, the differences between the classical and quantum-corrected enthalpy of adsorption are the largest. This is not surprising because

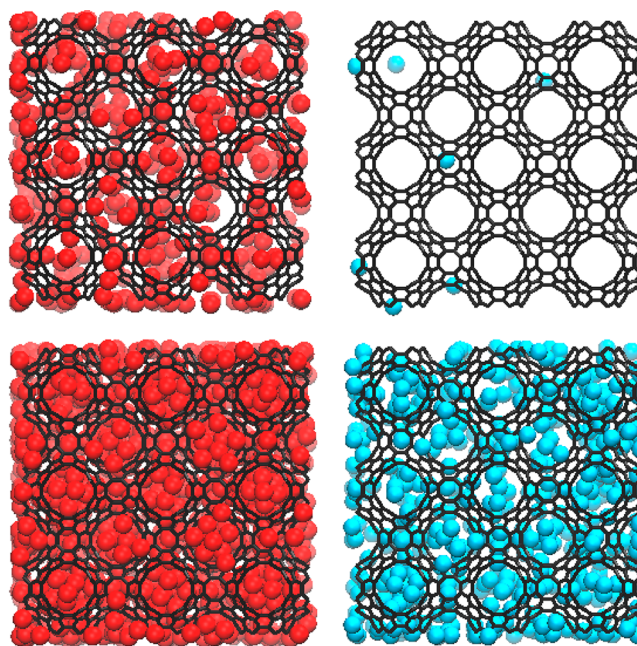


Figure 5. Snapshots of ^{20}Ne (left panel) and ^4He (right panel) adsorbed in Schwarz P-carbon sample at 10 (top panels) and 1080 kPa (bottom panels) at 77 K. Note the high packing of ^{20}Ne atoms compared to loosely packed ^4He ones.

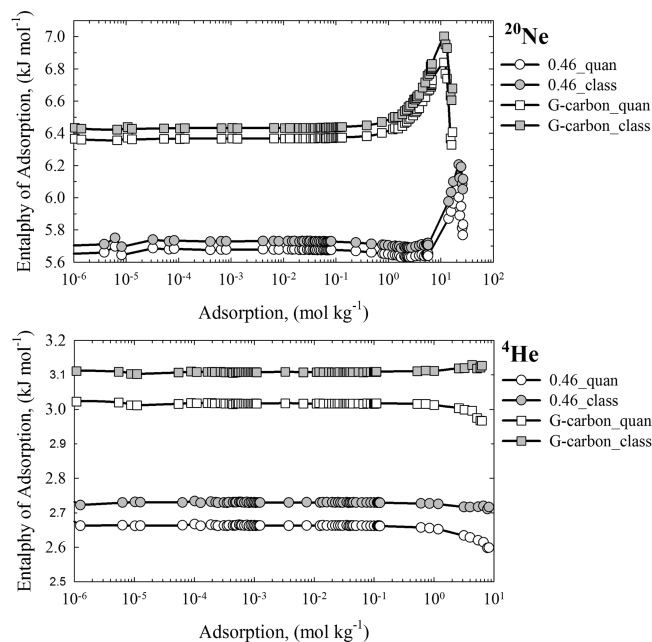


Figure 6. Classical (closed symbols) and quantum-corrected (open symbols) enthalpy of ^4He (bottom panel) and ^{20}Ne (upper panel) adsorption in the graphite-like lamellar nanostructure consisting of the smallest flat nanopores (i.e., $\Delta = 0.46$ nm) and Schoen G-carbon sample at 77 K. Note that quantum fluctuations decrease the heat realized during adsorption processes compared to classical results.

quantum effects are very high in narrow carbon nanopores due to localization in positional space.^{50,51} For the graphite-like lamellar nanostructure consisting of the smallest carbon nanopores, the quantum-corrected enthalpy of ^4He adsorption is lower by ~ 1 kJ mol⁻¹ compared to its classical counterpart at low pressures and 77 K. For heavier ^{20}Ne this difference is lower, i.e., ~ 0.5 kJ mol⁻¹ (see Figure 6).

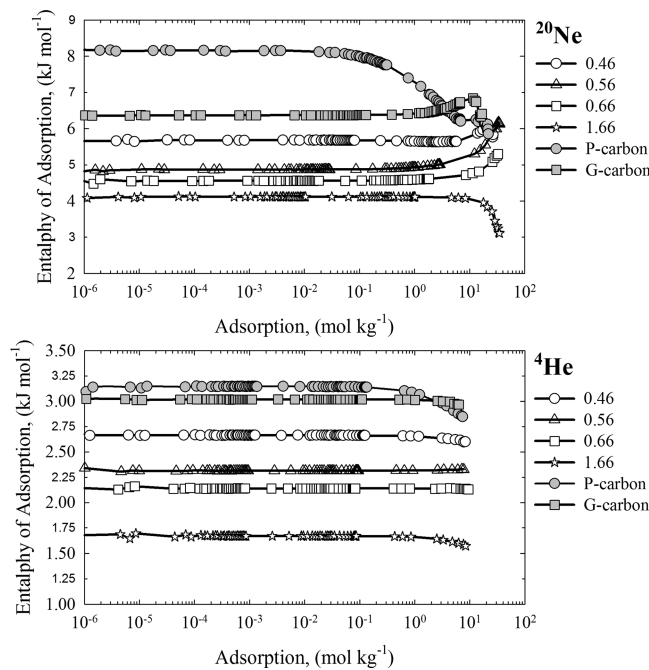


Figure 7. Quantum-corrected enthalpies of ^4He (bottom panel) and ^{20}Ne (upper panel) adsorption in Schwarz P-carbon, Schoen-G carbon, and selected graphite-like lamellar nanostructures at 77 K. The interlamellar distances, Δ , are displayed in the plots.

As would be expected, for both adsorbates the enthalpy of adsorption is the highest in triply periodic minimal carbon surfaces and graphite-like lamellar nanostructure consisting of narrow nanopores. The enhanced adsorption field in narrow flat/curved carbon nanopores is responsible for observed regularities (see Figure 7). Two interesting differences between the enthalpy of ^4He and ^{20}Ne are important. First, the enthalpy of ^{20}Ne adsorption is at least twice the enthalpy of ^4He adsorption at low pore loadings and 77 K. Second, the enthalpy of ^4He adsorption is pore-loading independent (except Schwarz P-carbon sample), whereas the enthalpy of ^{20}Ne adsorption is nonmonotonic and decreasing/increasing with pore loadings above 10 mol kg^{-1} . Weak adsorption of ^4He in studied carbonaceous nanomaterials at 77 K is responsible for the constant value of the adsorption enthalpy. In contrast, ^{20}Ne atoms are strongly adsorbed at studied operating conditions. Packing and compression of confined ^{20}Ne atoms impact the energy/particle fluctuations that increase/decrease the adsorption enthalpy, as is displayed in Figure 7. The equilibrium separation factor is high when the affinities of mixture components toward nanoporous material are significantly different. For Schwarz P-carbon sample, we found the largest difference of $\sim 5 \text{ kJ mol}^{-1}$ between the ^{20}Ne and ^4He adsorption enthalpy computed at low pore loadings. For Schoen G-carbon sample, adsorbed ^{20}Ne released around $\sim 3.3 \text{ kJ mol}^{-1}$ more heat than ^4He at low pore loadings. As would be expected, graphite-like lamellar nanostructures consisting of flat carbon nanopores are less selective toward ^{20}Ne . For $\Delta = 0.46 \text{ nm}$, the difference between the ^{20}Ne and ^4He adsorption enthalpy is around $\sim 3.0 \text{ kJ mol}^{-1}$ at low pore loadings. But for $\Delta = 1.66 \text{ nm}$, the heat released during ^{20}Ne adsorption is only 2.5 kJ mol^{-1} greater compared to the ^4He one. Therefore, it is clear that studied triply periodic minimal carbon surfaces are more selective carbonaceous nanomaterials than graphite-like lamellar nanostructures.

The equilibrium selectivity of ^{20}Ne over ^4He , $\alpha_{\text{Ne-He}}$, computed from IAST theory is shown in Figure 8. Pore size

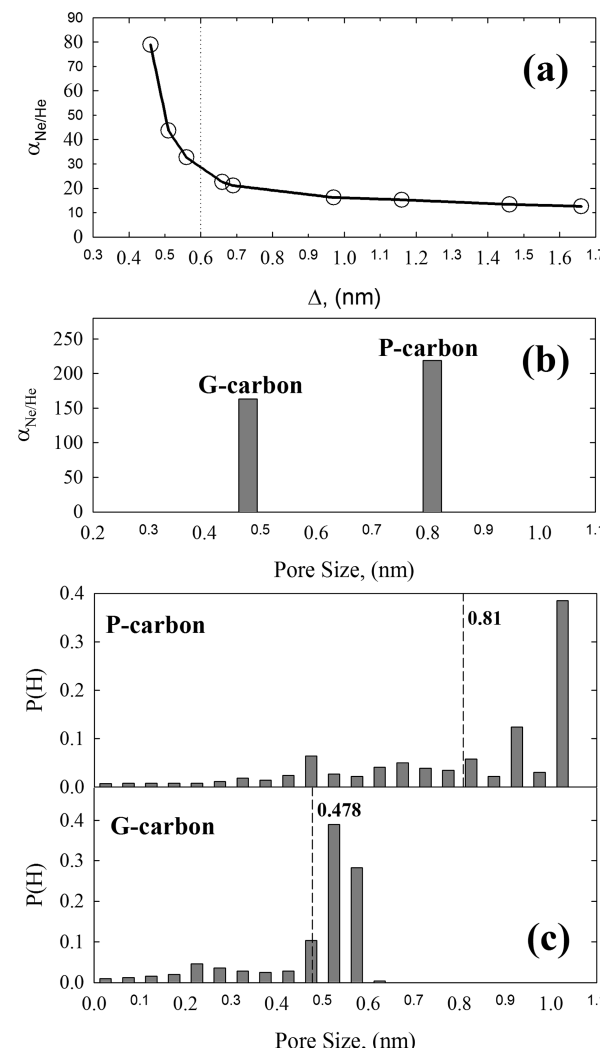


Figure 8. (a) Variation of equilibrium selectivity of ^{20}Ne over ^4He with interlamellar distances, Δ , computed for mixtures at infinite dilution. (b) $^{20}\text{Ne}/^4\text{He}$ equilibrium separation factor computed for studied triply periodic carbon minimal surfaces at infinite dilution (i.e., Schwarz P-carbon and Schoen G-carbon). (c) Pore size distributions of Schwarz P-carbon and Schoen G-carbon surfaces. Dashed lines display the average pore sizes.

distributions computed for Schwarz P-carbon and Schoen G-carbon samples are also attached. Studied triply periodic minimal carbon surfaces seem to be superior adsorbents for equilibrium separation of $^{20}\text{Ne}-^4\text{He}$ mixtures at 77 K and low pore loadings. Both carbonaceous nanomaterials have strong preference toward ^{20}Ne . For Schwarz P-carbon sample $\alpha_{\text{Ne-He}}$ approaches 219, whereas for Schoen G-carbon sample $\alpha_{\text{Ne-He}}$ is reduced up to 163. As would be expected, for graphite-like lamellar nanostructures, the separation factor at infinite dilution of adsorbed phase increases as the interlamellar distance is reduced. However, what is more important, we found that for $\Delta < 0.6 \text{ nm}$ (i.e., $2.15\sigma_{\text{Ne}}$ where σ_{Ne} denotes the LJ collision diameter for ^{20}Ne) the equilibrium selectivity increases exponentially. For $\Delta = 0.46 \text{ nm}$, $\alpha_{\text{Ne-He}}$ is high and reaches 80. The analysis of pore size distributions displayed in Figure 8 indicated that nanopore curvature is a key to get highly

selective adsorbent toward separation of noble gas mixtures at cryogenic temperatures. Note that the Schwarz P-carbon sample contains wider carbon nanopores compared to the Schoen G-carbon sample. Furthermore, these carbon nanopores are wider compared to flat ones characteristic for graphite-like lamellar nanostructures. Nevertheless, adsorption isotherms, enthalpies, and equilibrium selectivities clearly showed that Schwarz P-carbon sample is the most selective carbonaceous adsorbent among studied ones.

Note, however, that for potential industrial applications of these carbonaceous nanomaterials, high equilibrium selectivities for mixtures at finite pressures are necessary. Regardless of the nanopore size and topology, we found that the separation factor computed for the equimolar $^{20}\text{Ne}-^4\text{He}$ mixtures is still very high for total mixture pressure up to 1 kPa (see Figure 9). At

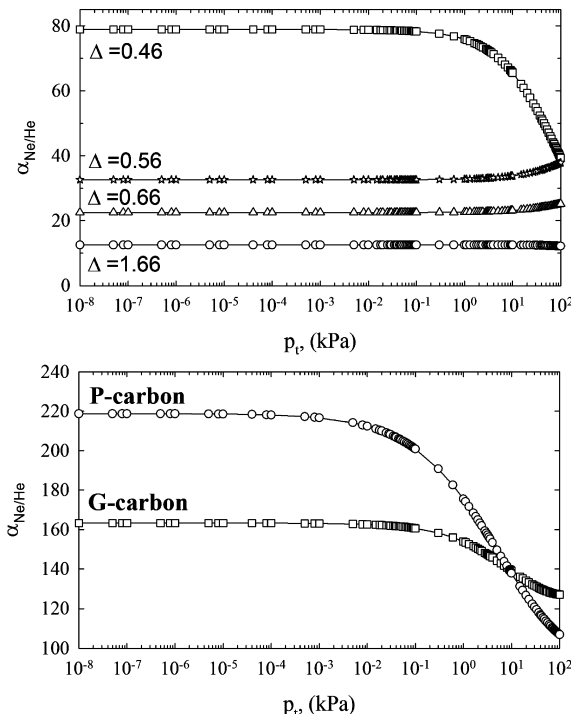


Figure 9. Upper panel: variation of equilibrium selectivity with the total pressure of equimolar $^{20}\text{Ne}-^4\text{He}$ mixtures at 77 K. The interlamellar distances, Δ , are displayed on the plots. Lower panel: variation of equilibrium selectivity with the total pressure of equimolar $^{20}\text{Ne}-^4\text{He}$ mixtures at 77 K computed for the Schwarz P-carbon and Schoen G-carbon.

higher p_t , the equilibrium selectivity is not constant. For triply periodic minimal carbon surfaces and graphite-like lamellar nanostructures consisting of the smallest flat nanopores (i.e., $\Delta = 0.46$ nm), the equilibrium separation factor is significantly reduced for $p_t > 1$ kPa. This is because ^4He atoms are coadsorbed at higher equimolar mixture pressures (see Figure 4 and 5). Below $p_t < 1$ kPa, the coadsorption of ^4He is negligible as can be inferred from the single-adsorption isotherms depicted in Figure 4. In graphite-like lamellar nanostructures consisting of wider carbon nanopores, the adsorption field is weaker. Therefore, $\alpha_{\text{Ne-He}}$ is either constant or weakly increasing. Further investigations are needed to fully explore the role of nanopore curvature in cryogenic separation of noble gas mixtures by physisorption.

IV. CONCLUSIONS

We investigated the adsorption and equilibrium separation of $^{20}\text{Ne}-^4\text{He}$ mixtures in Schwarz P-carbon, Schoen G-carbon, and series of graphite-like lamellar nanostructures at 77 K. The quantum nature of studied light atoms was captured by the Feynman–Kleinert–Séssé variational approach. The binary $^{20}\text{Ne}/^4\text{He}$ mixture adsorption was computed from the single-component adsorption isotherms via the ideal adsorbed solution theory. ^{20}Ne atoms bind stronger to curved as well as flat graphene planes as compared to ^4He ones, which results in preferential adsorption of heavier atoms. However, the effect of the carbon nanopore curvature seems to be the key to control the efficiency of noble gas mixture separation by cryogenic physisorption. The enthalpy of ^{20}Ne adsorption in Schwarz P-carbon sample reaches 8.15 kJ mol^{-1} at 77 K and low pore loadings. In contrast, the maximum heat released during ^4He physisorption in Schwarz P-carbon sample is 3.15 kJ mol^{-1} . As a result of this, the equilibrium selectivity of ^{20}Ne over ^4He computed at infinite mixture dilution is very high and reaches 219. For comparison, the equilibrium separation factor computed at the same operating conditions for Schoen G-carbon sample is 163. Because of the flat geometry of carbon nanopores, graphite-like lamellar nanostructures are less efficient adsorbents for separation of noble gas mixtures at 77 K. The maximum selectivity of ^{20}Ne over ^4He of ~ 80 can be achieved for the smallest interlamellar distance, i.e., $\Delta = 0.46$ nm. In wider flat carbon nanopores, the equilibrium selectivity is dropped to ~ 10 because of the fast reduction of surface forces. More importantly, we found that for all studied carbonaceous nanomaterials, the equilibrium separation factor computed for the equimolar $^{20}\text{Ne}-^4\text{He}$ mixtures is very high up to a total mixture pressure of 1 kPa. This circumstance is indicative of the possibility of carrying out the adsorption separation of $^{20}\text{Ne}-^4\text{He}$ mixtures at $p_t < 1$ kPa and 77 K that do not require high-energy consumption.

■ AUTHOR INFORMATION

Corresponding Author

*Tel.: +61 8 9266 7800. E-mail: Piotr.Kowalczyk@curtin.edu.au.

Notes

The authors declare no competing financial interest.

■ ACKNOWLEDGMENTS

P.K. acknowledges partial support by the Office of Research & Development, Curtin University of Technology, Grant CRF10084. P.K. acknowledges partial support by the Australian Academy of Science, Scientific Visits to Japan 2011-12. P.A.G. and A.P.T. acknowledge the use of the computer cluster at Poznan Supercomputing and Networking Centre and Networking Centre and the Information and Communication Technology Centre of the Nicolaus Copernicus University. P.K. acknowledges the use of the EPIC computer cluster (ivec.org.au). The authors gratefully acknowledge Reviewer 2 for stimulating comments and suggestions.

■ REFERENCES

- (1) Kerry, F. G. *Industrial Gas Handbook: Gas Separation and Purification*; CRC Press: Boca Raton, FL, 2007.
- (2) Scott, K. *Handbook of Industrial Membranes*; Elsevier Science Publishers LTD: Oxford, U.K., 1995.

- (3) Jha, A. R. *Cryogenic Technology and Applications*; Elsevier Inc.: Oxford, U.K., 2006.
- (4) Pauling, L. *The Nature of the Chemical Bond*; Cornell University Press: New York, 1960.
- (5) Thirumalai, D.; Hall, R. W.; Berne, B. J. *J. Chem. Phys.* **1984**, *81*, 2523–2527.
- (6) Wang, Q.; Johnson, J. K. *Fluid Phase Equilib.* **1997**, *132*, 93–116.
- (7) Sesé, L. M. *Mol. Phys.* **1995**, *85*, 931–947.
- (8) Sesé, L. M. *Mol. Phys.* **2002**, *100*, 927–940.
- (9) Sesé, L. M. *Mol. Phys.* **1994**, *81*, 1297–1312.
- (10) Kowalczyk, P.; Gauden, P. A.; Terzyk, A. P. *J. Phys. Chem. B* **2010**, *114*, 5047–5052.
- (11) Kowalczyk, P.; Brualla, L.; Gauden, P. A.; Terzyk, A. P. *Phys. Chem. Chem. Phys.* **2009**, *11*, 9182–9187.
- (12) Ceperley, D. M. *Rev. Mod. Phys.* **1995**, *67*, 279–356.
- (13) Ceperley, D. M. *Rev. Mod. Phys.* **1999**, *71*, S438–S443.
- (14) Kowalczyk, P.; Gauden, P. A.; Terzyk, A. P.; Furmaniak, S. *J. Chem. Theory Comput.* **2009**, *5*, 1990–1996.
- (15) Rabani, E.; Krilov, G.; Reichman, D. R.; Berne, B. J. *J. Chem. Phys.* **2005**, *123*, 184506–1–184506–7.
- (16) Kletenik-Edelman, O.; Reichman, D. R.; Rabani, E. *J. Chem. Phys.* **2011**, *134*, 044528–1–044528–10.
- (17) Morales, J. J.; Nuevo, M. J. *J. Comput. Chem.* **1995**, *16*, 105–112.
- (18) Poulsen, J.; Scheers, J.; Nyman, G.; Rossky, P. *Phys. Rev. B* **2007**, *75*, 224505–1–224505–9.
- (19) Berne, B. J.; Thirumalai, D. *Annu. Rev. Phys. Chem.* **1986**, *37*, 401–424.
- (20) Azuah, R.; Stirling, W.; Glyde, H.; Boninsegni, M. *J. Low Temp. Phys.* **1997**, *109*, 287–308.
- (21) Ramires, R.; Herrero, C. P. *J. Chem. Phys.* **2008**, *129*, 204502–1–204502–10.
- (22) Ramires, R.; Herrero, C. P.; Antonelli, A.; Hernandez, E. R. *J. Chem. Phys.* **2008**, *129*, 064110–1–064110–11.
- (23) Beenakker, J. J. M.; Borman, V. D.; Krylov, S. Y. *Chem. Phys. Lett.* **1995**, *232*, 379–382.
- (24) Tanaka, H.; El-Merraoui, M.; Kodaira, T.; Kaneko, K. *Chem. Phys. Lett.* **2002**, *351*, 417–423.
- (25) Kowalczyk, P.; Holyst, R.; Terrones, M.; Terrones, H. *Phys. Chem. Chem. Phys.* **2007**, *9*, 1786–1792.
- (26) Kowalczyk, P.; Tanaka, H.; Holyst, R.; Kaneko, K.; Ohmori, T.; Miyamoto, J. *J. Phys. Chem. B* **2005**, *109*, 17174–17183.
- (27) Ruthven, D. M.; Farooq, S.; Knaebel, K. S. *Pressure Swing Adsorption*; VCH Publishers Inc.: New York, 1994.
- (28) Ruthven, D. M. *Principles of Adsorption and Adsorption Processes*; John Wiley & Sons: New York, 1984.
- (29) Yang, R. T. *Gas Separation by Adsorption Processes*; Imperial Colleague Press: London, U.K., 1997.
- (30) Kowalczyk, P. *Phys. Chem. Chem. Phys.* **2012**, *14*, 2784–2790.
- (31) Karger, J.; Ruthven, D. M. *Diffusion in Zeolites and Other Microporous Solids*; John Wiley & Sons: New York, 1992.
- (32) Ungerer, Ph.; Tavitian, B.; Boutin, A. *Applications of Molecular Simulation in the Oil and Gas Industry. Monte Carlo Methods*; IFP Publications: Paris, France, 2005.
- (33) Chmiola, J.; Yushin, G.; Gogotsi, Y.; Portet, C.; Simon, P.; Taberna, P. L. *Science* **2006**, *313*, 1760–1763.
- (34) Asai, M.; Ohba, T.; Iwanaga, T.; Kanoh, H.; Endo, M.; Campos-Delgado, J.; Terrones, M.; Nakai, K.; Kaneko, K. *J. Am. Chem. Soc.* **2011**, *133*, 14880–14883.
- (35) Sesé, L. M. *Mol. Phys.* **1999**, *97*, 881–896.
- (36) Allen, M. P.; Tildesley, D. J. *Computer Simulation of Liquids*; Clarendon: Oxford, U.K., 1987.
- (37) Mackay, A.; Terrones, H. *Nature* **1991**, *352*, 762–762.
- (38) Nicholson, D.; Parsonage, N. G. *Computer Simulation and the Statistical Mechanics of Adsorption*; Academic Press: London, U.K., 1982.
- (39) Kowalczyk, P.; Gauden, P. A.; Terzyk, A. P.; Furmaniak, S. *Phys. Chem. Chem. Phys.* **2010**, *12*, 11351–11361.
- (40) Steele, W. A. *The Interaction of Gases with Solid Surfaces*; Pergamon Press: Oxford, U.K., 1974.
- (41) Feynman, R. P.; Kleinert, H. *Phys. Rev. A* **1986**, *34*, 5080–5084.
- (42) Widom, B. *J. Chem. Phys.* **1963**, *39*, 2808–2812.
- (43) Myers, A. L.; Prausnitz, J. M. *AIChE J.* **1965**, *11*, 121–127.
- (44) Valenzuela, D. P.; Myers, A. L. *Adsorption Equilibrium Data Handbook*; Prentice Hall Inc.: Upper Saddle River, NJ, 1989.
- (45) Toth, J. *Adsorption: Theory, Modeling, and Analysis*; Marcel Dekker: New York, 2002.
- (46) Challa, S. R.; Sholl, D. S.; Johnson, J. K. *J. Chem. Phys.* **2002**, *116*, 814–824.
- (47) Chandler, D.; Wolynes, P. G. *J. Chem. Phys.* **1981**, *74*, 4078–4095.
- (48) Vagraftik, N. B. *The Handbook of Thermodynamic Properties of Gases and Liquids*; GIFML: Moscow, Russia, 1963 (in Russian).
- (49) Sing, K. S. W.; Everett, D. H.; Haul, R. A. W.; Moscou, L.; Pierotti, R. A.; Rouquerol, J.; Siemieniewska, T. *Pure Appl. Chem.* **1985**, *57*, 603–619.
- (50) Kowalczyk, P.; Gauden, P. A.; Terzyk, A. P.; Bhatia, S. K. *Langmuir* **2007**, *23*, 3666–3672.
- (51) Kowalczyk, P.; Gauden, P. A.; Terzyk, A. P.; Furmaniak, S. J. *Phys.: Condens. Matter* **2009**, *21*, 144210–1–144210–12.